Chapter 13
Quantized Crystal Plasticity Modeling of Nanocrystalline Metals

Lin Li and Peter M. Anderson

13.1 Introduction

Nanocrystalline (NC) metals are often defined as polycrystalline metals with an average grain size less than 100 nm. Their appealing mechanical properties make them promising structural materials. Compared to coarse-grained (CG) counterparts, NC metals exhibit: (1) ultrahigh yield and fracture strength; (2) an extended elastic–plastic transition regime; (3) large recoverable plastic deformation; (4) high strain-rate sensitivity; and (5) limited ductility due to strain localization [1–3]. These unique features pertain to the physics of deformation that emerge as grain size decreases below ∼100 nm [4–6]. First, the plastic flow shifts from multiple to single dislocation slip. In stark contrast to CG metals, intragranular dislocation activities—including the operation of dislocation sources (e.g., Frank-Read) as well as dislocation multiplication and intersection—are highly prohibited. Instead, dislocations in NC metals tend to nucleate at grain boundaries (GBs) and traverse entire grains without impediment until they are absorbed into GBs. GB sites therefore act as sources and sinks for dislocations. If the grain size is refined below 10–20 nm, GB accommodation mechanisms (e.g., GB sliding and rotation) become more important and begin to control plastic flow [7, 8].

This chapter presents a quantized crystal plasticity (QCP) model that connects emerging deformation physics with the unique mechanical properties of NC metal

L. Li (✉)
Department of Metallurgical and Materials Engineering, The University of Alabama, Tuscaloosa, AL 35487, USA
e-mail: lin.li@eng.ua.edu

P.M. Anderson
Department of Materials Science and Engineering, The Ohio State University, Columbus, OH 43210, USA

C.R. Weinberger, G.J. Tucker (eds.), *Multiscale Materials Modeling for Nanomechanics*, Springer Series in Materials Science 245,
DOI 10.1007/978-3-319-33480-6_13

in the grain size regime between 20 and 100 nm, where single dislocation slip controls the plastic flow [9–12]. Notably, the QCP model adopts a discrete/quantized constitutive flow rule associated with a single dislocation slip event in a nano grain. The flow rule is implemented for a NC assembly within the framework of crystal plasticity. By calibrating the model to measurements of aggregate flow strength and internal stress within subpopulations of grains, we infer that the critical resolved shear stress (CRSS) for quantized slip is heterogeneous from one grain to another. The CRSS distribution is skewed (asymmetric) so that a larger fraction of low-strength grains is balanced by a smaller fraction of high-strength grains. Further, the CRSS of a grain depends on the grain size but not grain orientation. In Sect. 13.2 to follow, the QCP model is developed. In Sect. 13.3, the model is calibrated and validated under monotonic and cyclic mechanical loadings. In Sect. 13.4, the evolution of lattice strain with deformation in NC metals is explored by capturing the deformation footprints in in-situ X-ray diffraction tests. Section 13.5 summarizes the key aspects and motivates areas of future development.

13.2 Model Development

13.2.1 Dislocation Depinning from Grain Boundaries

Atomic simulations have provided considerable insight into the deformation mechanisms in NC metals [5, 13–15]. One of the emerging deformation processes is the nucleation and propagation of dislocations from grain boundaries [5]. In this process, dislocations often become pinned at GB ledges as they propagate across the grain. Thus, the rate-limiting process is the depinning of the dislocations and the characteristic length scale is the spacing between boundary pinning points. A molecular dynamics (MD) simulation of three-dimensional NC Al with an averaged grain size $\sim$12 nm was performed at a constant strain rate 1×10^8 s^{-1} and at a constant temperature 300 K. The simulated sample consisted of 100 grains, and periodic boundary conditions were applied to all the three directions. The embedded atom model potential for Al of Mishin et al. [16] was used, it has an unstable-to-stable stacking fault energy ratio close to unity, so that the nucleation of trailing partial dislocations after the leading partial dislocation can be observed within the time frame of the MD simulation. The simulated results were analyzed in terms of grain-averaged shear produced by dislocation slip and the grain-averaged resolved shear stress during deformation [17]. Figure 13.1a–c illustrates three crucial snapshots from the MD simulations and Fig. 13.1d shows the corresponding evolution of resolved shear stress and strain within a grain, measured on a grain-averaged basis. A full dislocation loop is observed to persist in a pinned, embryonic state for 25 ps (Fig. 13.1a) until the grain-averaged stress τ reaches a critical value (Fig. 13.1b). The full dislocation then depins from the GB obstacles and sweeps across the grain (Figs. 13.1b, c). The grain-averaged shear γ^* then increments by a

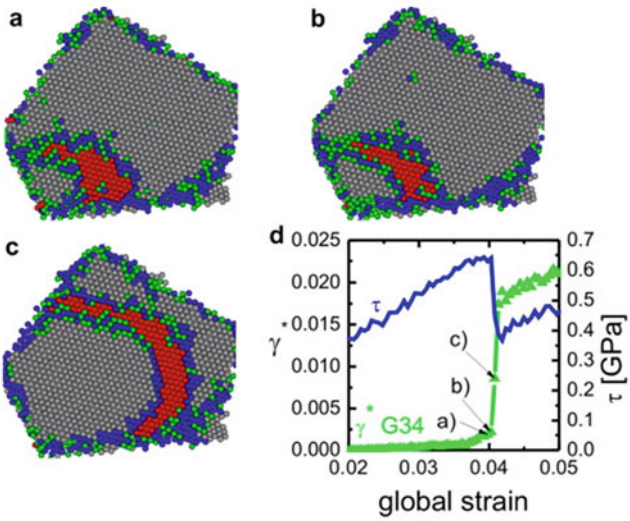

Fig. 13.1 Molecular dynamics simulations of a cross section of an FCC Al crystal. With increasing applied deformation, a perfect dislocation consisting of two partials depins from a GB ledge [17]. (**a**–**c**) Shows a cut through a selected grain with the atoms colored according to their local crystallographic order. Atoms with an FCC environment are colored in *grey*, those with HCP are *red*, others with coordination = 12 are *green*, and those with coordination ≠ 12 are *blue*. (**d**) Shows the corresponding evolution of grain-averaged shear γ^* and resolved shear stress τ. Reprinted figure from [17] with permission from Elsevier

discrete amount and the resolved shear stress τ simultaneously drops abruptly due to load shedding (Fig. 13.1d).

The grain-averaged analysis obtained from MD simulations highlights the quantized/discrete jumps in grain-averaged resolved shear stress and strain in nanoscale grains. Furthermore, the distribution of the depinning stress (CRSS) controls the onset of avalanches consisting of numerous quantized slip events. A statistical analysis of dislocation slip processes reveals a broad CRSS distribution that peaks between 600 and 700 MPa. Slip processes are seldom observed in a grain if the average resolved shear stresses in the grain is <500 MPa [17]. These MD observations of dislocation slip in nano grains motivate our meso-scale, QCP model. It is noteworthy that the MD simulations have the limits of grain sizes and the deformation strain rates that would be comparable to experimentally relevant values. The QCP model, therefore, adopts the quantized and stochastic single dislocation slip features, performs simulations at meso-scale level, and calibrates the characteristics of quantized slip with experimental measurements.

13.2.2 A Constitutive Model for Quantized Dislocation Slip in Nanoscale Grains

The QCP model employs a conventional crystal plasticity formulization [18, 19], the details of which can be found in Chap. 3. We augment the conventional crystal plasticity such that the increments in plastic shear strain take on discrete/quantized values and increase in magnitude as grain size decreases to the nanoscale. In this section, the detailed development of the QCP model and its implementation into the finite element method (FEM) are described.

Large-deformation kinematics are incorporated into the constitutive framework because these discrete events can impart plastic strain increments $\sim$1 %. Following [20], an infinitesimal vector $\mathbf{dX}$ in an undeformed (reference) configuration is distorted into a vector $\mathbf{dx} = \mathbf{FdX}$ in a deformed configuration. Here, the deformation gradient

$$\mathbf{F} = \mathbf{F}^{*}\mathbf{F}^{\mathbf{p}} \tag{13.1}$$

is multiplicatively decomposed into an elastic part $\mathbf{F}^{*}$ and a plastic part $\mathbf{F}^{\mathbf{p}}$. The elastic strain is defined as

$$\mathbf{E}^{*} = \frac{\mathbf{1}}{\mathbf{2}}\left\{\mathbf{F}^{*^{\mathbf{T}}}\mathbf{F}^{*} - \mathbf{I}\right\} \tag{13.2}$$

The stress at a material point is given by

$$\mathbf{T}^{*} = \mathbf{C}\mathbf{E}^{*} \tag{13.3}$$

Here, $\mathbf{C}$ is the fourth-order elasticity tensor for a grain. For FCC materials, there are only three independent constants and they are traditionally denoted by C_{11}, C_{12}, and C_{44} within the cubic crystal basis. $\mathbf{T}^{*}$ is the symmetric Piola-Kirchhoff stress, which is the work conjugate to $\mathbf{E}^{*}$. It is related to the Cauchy stress $\mathbf{T}$ by

$$\mathbf{T}^{*} = \mathbf{det}\left(\mathbf{F}^{*}\right)\mathbf{F}^{*^{-1}}\mathbf{T}\mathbf{F}^{*^{-\mathbf{T}}} \tag{13.4}$$

The time evolution equation for $\mathbf{F}^{\mathbf{p}}$ is given by flow rule

$$\dot{\mathbf{F}}^{\mathbf{p}} = \mathbf{L}^{\mathbf{p}}\mathbf{F}^{\mathbf{p}} \tag{13.5}$$

with

$$\mathbf{L}^{\mathbf{p}} = \sum_{\alpha}\dot{\boldsymbol{\gamma}}^{\alpha}\mathbf{S}_{\mathbf{0}}^{\alpha}, \quad \mathbf{S}_{\mathbf{0}}^{\alpha} = \mathbf{s}_{\mathbf{0}}^{\alpha} \otimes \mathbf{m}_{\mathbf{0}}^{\alpha} \tag{13.6}$$

The orthonormal vector pairs $(\mathbf{s_0^\alpha}, \mathbf{m}_0^\alpha)$ define the respective slip direction and slip plane normal for slip system α. For FCC materials, $\mathbf{S_0^\alpha}$ is chosen to be 1 of the 12 $\langle 110\rangle/\{111\}$ slip systems. The shear rate $\dot{\gamma}^\alpha$ is determined by a constitutive relation of the form $\dot{\gamma}^\alpha = \widehat{\dot{\gamma}}^\alpha \left(\tau^\alpha,\ \tau_c^\alpha\right)$, where the resolved shear stress τ^α is determined by

$$\tau^\alpha = \mathbf{s_0^\alpha} \cdot \left(\mathbf{F}^{*\mathbf{T}}\mathbf{F}^*\mathbf{T}^*\right)\mathbf{m_0^\alpha} \tag{13.7}$$

and τ_c^α is the CRSS for a slip event. An initial assumption is that τ_c^α at a material point is the same for all 12 slip systems and remains constant with deformation (denoted by τ_c for brevity).

The discrete jumps in shear strain as a result of dislocation depinning from GBs observed in the MD simulations (ref. to Fig. 13.2a) can be rationalized in terms of the grain-averaged increment in plastic strain. In particular, the discrete/quantized shear increment γ_{target} associated with a single dislocation gliding on slip system α across a grain with grain size d can be expressed as

$$\Delta\gamma^\alpha = \gamma_{\text{target}} = \frac{A_s b}{V_g} = g\frac{b}{d} \tag{13.8}$$

where b is the Burger vector magnitude of the dislocation, A_s is the cross sectional area of the slip plane, V_g is volume of the grain, and g is a geometric factor. In principle, γ_{target} depends on the specific glide plane and the grain shape. These factors are incorporated into g. For example, $g = 1.5$ for a center-cut glide plane within a spherical grain and $g = 1.2$ for the maximum cross sectional area of a cubic grain with edge length d. Furthermore, when multiple slip events occur on slip system α, the accumulated shear strain takes on a quantized value of γ_{target}, given as

$$\gamma^\alpha = q\gamma_{\text{target}} \tag{13.9}$$

The coefficient $q = 1, 2$, etc., is an integer that characterizes the quantized plastic state.

The discrete or quantized nature of slip in Eq. (13.8) is implemented via a modification to conventional kinetic flow law proposed by Peirce et al. [21]. In particular, the rate of plastic shear strain on the 12 FCC $\langle 110\rangle/\{111\}$ slip systems is specified by

$$\dot{\gamma}^\alpha = \begin{cases} \dot{\gamma}_0 \left|\dfrac{\tau^\alpha}{R\tau_c}\right|^{1/m} \text{sign}\left(\tau^\alpha\right) & \text{inactive slip} \\ \dot{\gamma}_0 \text{sign}\left(\tau^\alpha\right) & \text{active slip} \end{cases} \tag{13.10}$$

where $\dot{\gamma}_0$ is the local reference shear rate of slip. The *inactive slip condition* on slip system α applies when $|\tau^\alpha| < \tau_c$. Equation (13.10) differs from a standard flow law formalism in that a coefficient R has been inserted to reinforce a numerically

inactive condition and also τ_c remains constant with deformation. The coefficient R is determined such that if an inactive slip condition applies, then $\dot{\gamma}^{\alpha} < 10^{-20}\dot{\gamma}_0$ so that grains deform primarily by anisotropic elasticity. For instance, if the power-law exponent $m = 0.1$ is chosen, then the numerically inactive condition is satisfied by selecting $R \sim 100$, which approximates the value of τ_c expressed in MPa, i.e., $R = \tau_c$/MPa. The use of the modified power function with R and m can avoid a numerical issue when $\dot{\gamma}^{\alpha}$ transitions upon activation of a quantized slip event. The *active slip condition* for slip system α applies if the condition $|\tau^{\alpha}| \geq \tau_c$ is met. It prevails until the grain-averaged resolved shear strain γ^{α} achieves the quantized amount, $\gamma_{\text{target}} \cdot \text{sign}(\tau^{\alpha})$, even if load shedding from the deforming grain causes $|\tau^{\alpha}| < \tau_c$ to occur before γ^{α} reaches the target value. A propagation condition is imposed to ensure that τ^{α} on the active slip system does not change sign during a slip event. During the active condition, $\left|\dot{\gamma}^{\alpha}\right| = \dot{\gamma}_0$, where $\dot{\gamma}_0 > 10\dot{\varepsilon}_{\text{global}}$ is required to ensure that the increment in macroscopic strain on the polycrystal is negligible during the course of a local slip event.

13.2.3 Statistical Distribution of Critical Stress of Quantized Slips

In addition to quantized plasticity, the QCP model adopts a grain-to-grain variation in the CRSS τ_c at which a quantized plastic event is triggered. Such a variation is suggested by the MD simulation results [17], in which a very broad distribution of grain-level critical stress is observed in the simulated nanocrystals. In principle, τ_c depends on numerous factors including the detailed structure of the bounding GBs, the orientation of slip planes to the GBs, elastic anisotropy, and the accommodation of incoming or outgoing dislocation content within GBs [5, 14, 17, 22]. In the absence of a deterministic relationship between τ_c and GB structure, two types of probability distribution functions for τ_c are explored. **Type S** is a normal distribution with probability density

$$\rho\left(\tau_c; \mu, \sigma\right) = \frac{1}{\sigma\sqrt{2\pi}} \exp\left(-\frac{\left(\tau_c - \mu\right)^2}{2\sigma^2}\right) \tag{13.11}$$

where μ is the mean value and σ^2 is the variance. **Type A** is a gamma distribution with probability density

$$\rho\left(\tau_c; k, \theta, \tau_{\min}\right) = \left(\tau_c - \tau_{\min}\right)^{k-1} \frac{\exp\left(-\left(\tau_c - \tau_{\min}\right)/\theta\right)}{\Gamma(k)\theta^k} \tag{13.12}$$

where k is a shape parameter, θ is a scale parameter, and $\tau_{\min}$ is a reference value below which $\rho(\tau_c) = 0$. The corresponding mean and variance are $\tau_{\min} + k\theta$ and $k\theta^2$, respectively. These two types differ in skewness. The Type S normal

distribution is symmetric about the mean value with skewness = 0 whereas the Type A gamma distribution is asymmetric and positively skewed (i.e., the tail at larger τ_c is longer than at smaller τ_c). The skewness of the gamma distribution is $2/k$ and therefore the gamma distribution approaches a normal distribution as k increases.

The stochastic nature of τ_c and its effect on the mechanical properties (e.g., strength) of NC metals have been reported experimentally [23–26]. However, the correlation with GB structure or GB network structure and the evolution with deformation are open issues that require future investigation. In Sect. 13.4, the relation between τ_c and grain orientation is investigated by calibrating $\rho(\tau_c)$ in the QCP model to capture in-situ X-ray diffraction measurements in NC Ni.

13.2.4 Propagation Condition

A *propagation condition* for a slip event imposes a lower bound on τ_c or equivalently an upper bound on γ_{target}. It is based on the physical requirement that the resolved shear stress in a grain does not change sign during a slip event. The purpose is to ensure sufficient stress to complete the expansion of the loop. An Eshelby-inclusion analysis [27, 28] indicates that a transformation strain γ_{target} in an ellipsoidal region will induce a stress drop

$$\Delta\tau = c\Delta\tau^{\text{Eshelby}} = -cM\gamma_{\text{target}}; \quad M = \mu \cdot \frac{7-5\nu}{15\cdot(1-\nu)} \tag{13.13}$$

where μ and ν are the elastic shear modulus and Poisson's ratio of a homogeneous, isotropic-elastic medium, respectively. A parameter c is introduced to calibrate the deviation of non-ellipsoidal region in an elastic anisotropic medium to the Eshelby solution.

The propagation condition that the resolved shear stress of an active slip event does not change sign can be applied to Eq. (13.13), given

$$\tau_{\text{c}} \geq cM\gamma_{\text{target}} \text{ or equivalently, } \gamma_{\text{target}} \leq \tau_{\text{c}}/cM \tag{13.14}$$

Upon implementation, the geometric prescription for γ_{target} (Eq. (13.8)) is generally applied for a given grain and slip plane geometry. Experimentally measured stress–strain responses are used to parameterize τ_c distribution. Sometimes for small grain sizes (e.g., $d < 50$ nm) in particular, the fitted τ_c distribution has a small population (<20 %) that does not satisfy the propagation condition given in Eq. (13.14). For such small populations, the value of γ_{target} is adjusted to satisfy Eq. (13.14) using the prescribed value of τ_c. In practice, γ_{target} for a given grain is specified by the minimum,

$$\gamma_{\text{target}} = \min\left(\frac{\tau_{\text{c}}}{cM}, g\frac{b}{d}\right) \tag{13.15}$$

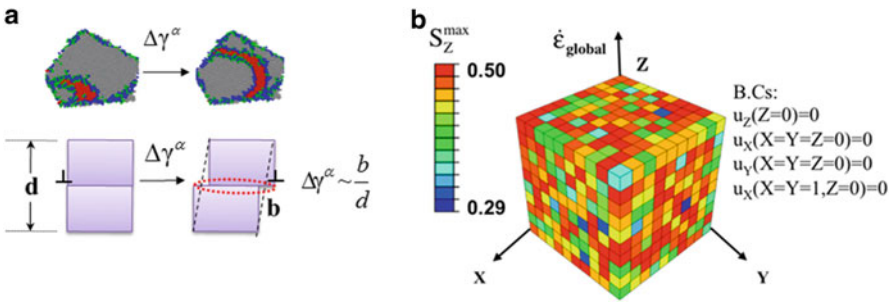

Fig. 13.2 (**a**) A schematic representation of coarse-graining dislocation depinning in the QCP model. (**b**) A finite element model of a polycrystal with $10 \times 10 \times 10$ grains, each represented by an 8-node brick element. Uniaxial tension is applied along the z-direction. Each grain is colored according to $S_z^{\max}$ the maximum Schmid factor among the 12 FCC slip systems in that grain. Numerical values are as shown in color bar

where τ_c is chosen from a statistical distribution following Eqs. (13.11) or (13.12).

13.2.5 QCP/FE Simulations

The QCP model is implemented in the commercial finite element (FE) packet ABAQUS via a user defined material subroutine (UMAT) [29]. A three-dimensional (3D) polycrystal is defined with $N \times N \times N$ grains, each represented by an 8-node, 3D cubic element (type = C3D8). A crystallographic orientation, CRSS τ_c and quantized plastic strain jump γ_{target} are assigned to each grain. Figure 13.2b shows a FE sample for $N = 10$ in which each grain (element) is colored according to the maximum Schmid factor with respect to the loading axis among the 12 ½⟨110⟩/{111} face-centered cubic (FCC) slip systems. A uniaxial strain rate $\dot{\varepsilon}_{\text{global}}$ is imposed via a constant displacement rate $\dot{u}_Z$ applied normal to the $+Z$ (top) surface while $u_Z = 0$ is imposed on the $-Z$ (bottom) surface. The tractions $t_X = t_Y = 0$ are imposed on these surfaces and the remaining $\pm X$ and $\pm Y$ surfaces are traction-free, as shown in Fig. 13.2b.

13.3 Model Calibration

13.3.1 Quantized Jumps in Shear Strain and Stress

The QCP simulation results capture the quantized jumps in shear strain and stress at grain level. Figure 13.3 shows the resolved shear strain γ^α and resolved shear stress τ^α vs. global plastic strain $\varepsilon^p{}_{\text{global}}$, for a slip system with a moderate Schmid

factor $S_Z{}^{\alpha} = 0.465$ at a material point in an interior grain. The grain takes different quantized states of γ^{α}, and jumps from one state to another when the resolved shear stress reaches a critical value. The black stepped (lower) trace shows that γ^{α} jumps successively by γ_{target} ($=4 \times 10^{-3}$). The red (upper) trace confirms that γ^{α} jumps when $\tau^{\alpha} = \tau_c$ (=500 MPa). During a jump by γ_{target}, τ^{α} monotonically decreases, reaching a minimum at the completion of the jump. Subsequently, τ^{α} monotonically increases via elastic deformation as the applied macroscopic strain increases. Occasionally, τ^{α} drops abruptly (arrow A) or deviates from linearity (arrow A′), even though slip system α is not active. This is a consequence of slip events in adjoining grains or sometimes in the same grain. Quantized slip is therefore predicted to generate violent redistributions of stress at the grain scale. This captures the key features of dislocation slip and depinning processes as observed in MD simulations.

13.3.2 Grain Size Effect on Strength

Plastic strengthening with decreasing grain size emerges as a consequence of quantized slip and the associated propagation condition. Figure 13.4a displays the evolution of resolved shear strain γ^{α} for discrete values of γ_{target}. The corresponding traces of τ^{α} vs. $\varepsilon^{p}{}_{\text{global}}$ for $\gamma_{\text{target}} = 1 \times 10^{-4}$ and 6×10^{-3} are shown in Fig. 13.4b, c, respectively. The stress redistribution in τ^{α} is more violent for the larger γ_{target} case. In particular, the stress drop $\Delta\tau$ due to a quantized slip event increases as γ_{target} increases. Figure 13.4d shows that $\Delta\tau$ increases linearly with γ_{target} with a slope of 65 GPa. This is consistent with the Eshelby solution (Eq. (13.13)) with $c = 1.6$, $\mu = 76$ GPa, and $\upsilon = 0.31$ for Ni. Since γ_{target} is linearly dependent on 1/grain size (Eq. (13.15)), $\Delta\tau$ therefore scales as 1/grain size. In the limit of large grain size, both γ_{target} and $\Delta\tau$ diminish and the QCP model reverts to a conventional, elastic-perfectly plastic crystal plasticity model. In the limit of small grain size, the *propagation condition* requires that $\tau_c \geq \Delta\tau$. Combining Eqs. (13.8) and (13.13),

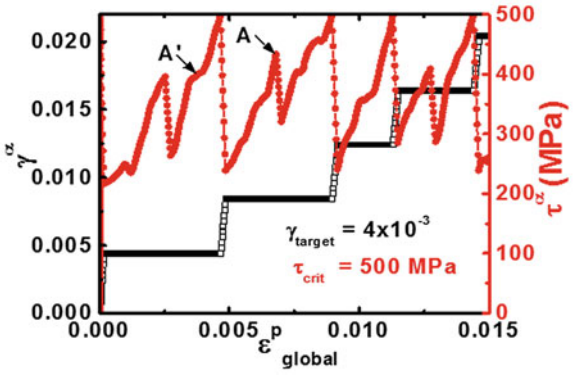

Fig. 13.3 The "quantized" evolution of local shear strain and the associated violent stress redistribution in shear stress at a material point of an interior grain with $\gamma_{\text{target}} = 4 \times 10^{-3}$ and $\tau_c = 500$ MPa. The elastic constants of Ni are used. Figure reproduced from [9]

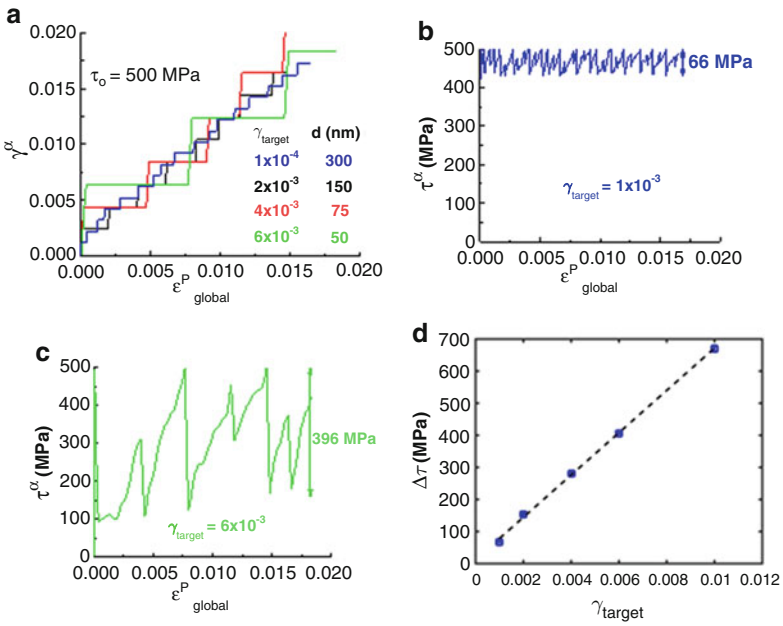

Fig. 13.4 (**a**) Evolution of plastic shear strain γ^α at a material point in an interior grain with various values of γ_{target} and $\tau_c = 500$ MPa. The corresponding evolution of resolved shear stress τ^α for $\gamma_{\text{target}} = 1 \times 10^{-4}$ and 6×10^{-3} are shown in (**b**, **c**), respectively. (**d**) The stress drop after a quantized slip $\Delta\tau$ vs. γ_{target}. The resulting linear relationship follows the prediction of Eq. (13.13), with $c = 1.6$, $\mu = 76$ GPa, and $\upsilon = 0.31$ for Ni. Figure (**a**–**c**) reproduced from [9]

we obtain

$$\tau_{c(\min)} = cM\gamma_{\text{target}} = c'\mu \cdot \frac{7 - 5\nu}{15 \cdot (1 - \nu)} \frac{b}{d} \tag{13.16}$$

where $c = 1.6$, $M = 40$ GPa, and $c' = 1.92$ for Ni. This is the origin of source strengthening with decreasing grain size in the QCP model. The resultant $1/d$ relationship differs from the $1/d^{½}$ dependence in the Hall–Petch relationship for conventional polycrystals [30, 31].

13.3.3 Extended Micro-Plasticity in NC Metals

The QCP model requires a valid distribution $\rho(\tau_c)$, and this can be achieved by fitting the experimental tensile stress–strain response for various average grain sizes. A particular goal is to reproduce the extended experimental micro-plastic regime, which is hypothesized to represent the percolation of quantized slip events

throughout the polycrystal, from soft to hard grains. The extended regime is quantified by $\varepsilon_{p(\text{trans})}$, the elastic–plastic transition strain over which the flow stress increases from an initial value σ_0 to approximately 95 % of the plateau stress σ_{plateau}. $\varepsilon_{p(\text{trans})} \sim 0.2\,\%$ for polycrystals with a conventional average grain size but it can approach 1 % for NC metals and exhibit apparent strain hardening under tension in this regime [32–34].

Figure 13.5a displays the fitted QCP simulation results for grain size $d = 50$, 150, 300 nm along with the experimental data for electro-deposited Ni from [35]. Two candidate distributions are considered for $\rho(\tau_c)$: a normal distribution (Fig. 13.5b, Eq. (13.11)) and a gamma distribution with the shape factor $k = 1$ (Fig. 13.5c, Eq. (13.12)) and $k = 2$ (Eq. (13.12)). The quantities to be calibrated (e.g., $\tau_{c(\text{min})}$, $\tau_{c(\text{mean})}$) are estimated from the experimental values of initial yield stress σ_0 and saturated flow stress σ_{plateau}. Iterative QCP simulations are performed to determine the values of $\tau_{c(\text{min})}$ and $\tau_{c(\text{mean})}$ that produce the best match to the data in Fig. 13.5a. The gamma distribution with $k = 1$ captures the gradual elastic-to-plastic transition, with $\varepsilon_{p(\text{trans})} = 0.7\,\%$ for $d = 50$ nm. These distributions are asymmetric and are denoted by "Type A" in Fig. 13.5a. In contrast, the normal distributions are symmetric and denoted by "Type S." They predict too small a transition, with $\varepsilon_{p(\text{trans})} = 0.08\,\%$ for $d = 50$ nm. The fitting process is detailed in [9] and the material and computational parameters are summarized in Table 13.1.

Figure 13.5c–e shows the gamma, $k = 1$ (Type A) $\rho(\tau_c)$ distributions that best fit the experimental data for various grain sizes. Both the mean value and standard deviation in τ_c increase with decreasing grain size. This reflects that yield in NC metals is very heterogeneous on a grain-to-grain scale. Moreover, the τ_c distribution becomes more asymmetric/skewed with decreasing grain size. In the limit of larger grain size, on the other hand, a gamma distribution with either $k = 1$ and $k = 2$ captures the experimental stress–strain data for $d = 300$ nm.

The QCP simulations predict that deformation is more localized as grain size decreases. Figure 13.6 shows the fraction (f_{slipped}) of grains with at least one slip event as a function of applied macro strain, as predicted by the calibrated QCP simulations. At smaller grain size ($d = 50$ nm), f_{slipped} increases gradually, indicating that plastic flow percolates gradually through the polycrystal. This produces the extended micro-plastic regime in Fig. 13.5a. At larger grain size ($d = 300$ nm), f_{slipped} is predicted to increase more rapidly with applied strain, consistent with more conventional crystal plasticity models. Compared to metals with a conventional grain size, NC metals accommodate global strain with larger local plastic strain events that are distributed among fewer grains; in other words, plastic deformation in NC metals tends to localize in fewer grains. For example, f_{slipped} at 0.2 % strain is $\sim$40 % for $d = 50$ nm but $\sim$80 % for $d = 300$ nm. Thus, a conventional 0.2 % macro plastic strain can capture fully plastic flow at larger grain size ($d = 300$ nm) but not at smaller grain size ($d = 50$ nm) [32–34].

Table 13.1 Summary of material and computational parameters employed by QCP simulations

Ni elastic moduli [55] (GPa)	C_{11}: 246.5	C_{12}: 147.3	C_{44}: 124.7
Crystal texture	Random with average maximum Schmid factor = 0.45		
Ave. grain size d (nm)	50	150	300
Crit. stress distribution (MPa): $\rho(\tau_c; k, \theta, \tau_{\min}) = (\tau_c - \tau_{\min})^{k-1} \frac{\exp(-(\tau_c - \tau_{\min})/\theta)}{\Gamma(k)\theta^k}$	$k = 1$ $\theta = 420$ $\tau_{c(\min)} = 280$	$k = 1$ $\theta = 285$ $\tau_{c(\min)} = 160$	$k = 1$ $\theta = 110$ $\tau_{c(\min)} = 80$
Quantized plastic strain: $\gamma_{\text{target}} = \min(\tau_c/60, 1.2\, b/d)$	$\gamma_{\text{target(min)}} = 4.7 \times 10^{-3}$ $\gamma_{\text{target(max)}} = 6.0 \times 10^{-3}$	2.0×10^{-3}	1.0×10^{-3}
Computational parameters	$\dot{\gamma}_0$ (s^{-1}): 2×10^{-2}	m: 0.1	Δt: $\gamma_{\text{target, max}}/\dot{\gamma}_0$

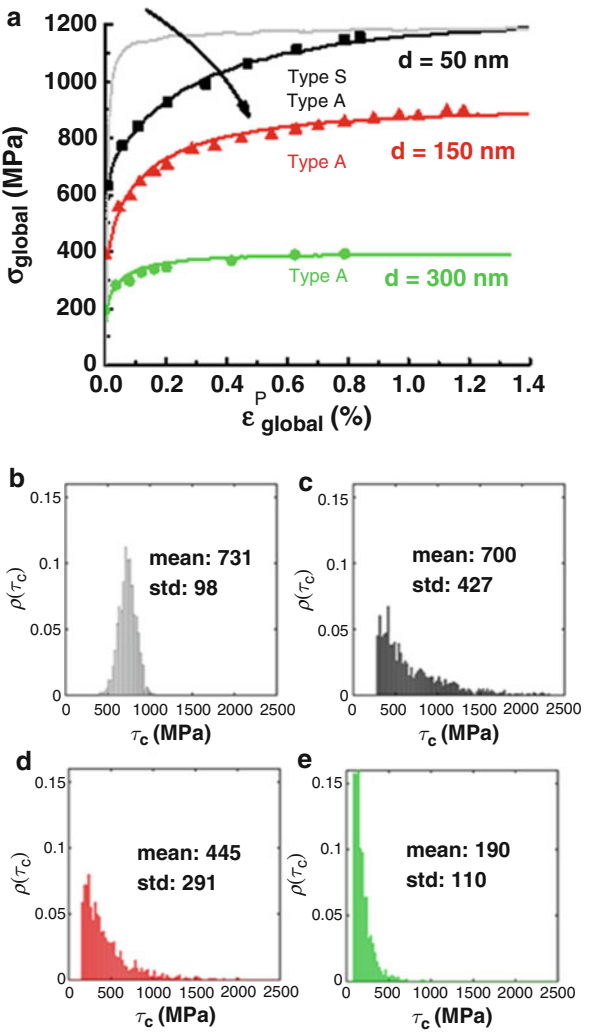

Fig. 13.5 (**a**) The simulated stress–strain responses for various grain sizes, along with the experimental data adopted from [35]. (**b**) A Type S (symmetric normal) distribution for $d = 50$ nm. (**c**–**e**) The best-fit Type A (asymmetric gamma, with $k = 1$) distributions for $d = 50$ nm, 150 nm and 300 nm, respectively. Figure reproduced from [9]

13.3.4 Enhanced Plastic Recovery

An asymmetric $\rho(\tau_c)$ distribution for NC metals is also supported by cyclic stress–strain data, in which an enhanced plastic recovery is usually observed [36–39]. The QCP model predicts reversible plastic strain to occur when NC metals are unloaded [10]. This arises when backward (or reverse) quantized slips occur in grains in which the resolved shear stress reverses sign and reaches a critical value $\tau_{c,b}$ for backward slip. Figure 13.7 shows the evolution of γ^α and τ^α on slip system α at a material point within a grain during macroscopic cyclic loading of a polycrystal. Here, $\gamma_{\text{target}} = 6 \times 10^{-3}$, $\tau_c = 428.4$ MPa, and $\tau_{c,b} = 228.4$ MPa. The

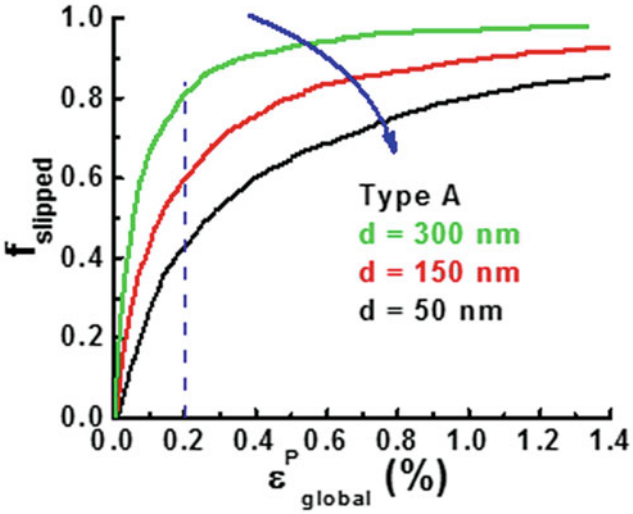

Fig. 13.6 The predicted fraction of slipped grains vs. macroscopic strain during a tension test, for various grain sizes. The QCP simulations use the best-fit Type A distributions in Fig. 13.5. Figure reproduced from [9]

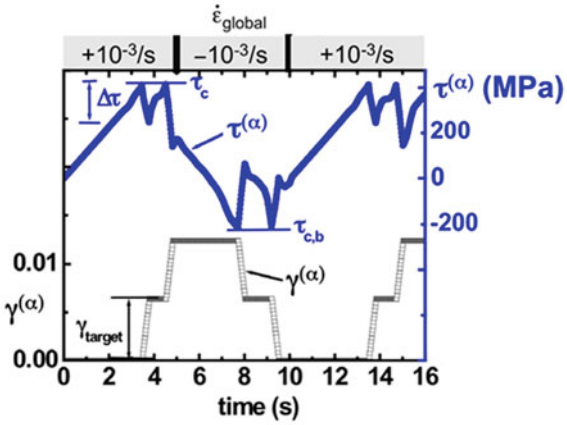

Fig. 13.7 Predictions of local shear strain γ^{α} (lower curve) and local resolved shear stress τ^{α} on a specific slip system α in an interior grain, as a function of time during a tension test. The applied global strain rate reverses sign at 5 and 10 s. Figure reproduced from [10]

smaller magnitude of $\tau_{c,b}$ signifies the case in which the pinning strength to reverse a quantized slip event is smaller than that for the initial forward event. For instance, deposition of the dislocation loop into a grain boundary could be energetically unfavorable, so that there is a driving force to reverse the process. During the first loading period, τ_c is reached twice so that the quantized slip number q increases from 0 to 1 and then 1 to 2. During the first unloading period, $-\tau_{c,b}$ is reached twice so that q decreases from 2 to 1 and then 1 to 0. During the second loading period, two forward events also occur and they produce $q = 2$.

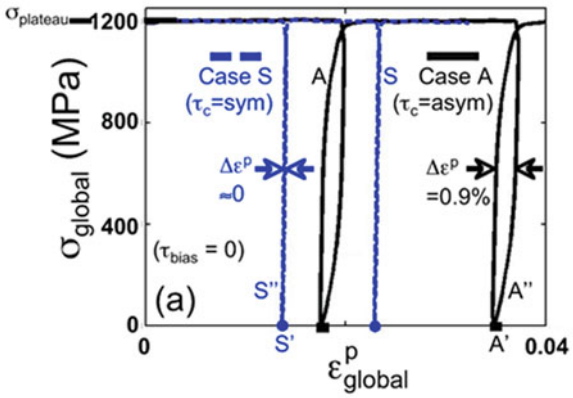

Fig. 13.8 (**a**) Predicted cyclic stress-plastic strain response of NC metals with $d = 50$ nm at large strain, using the Type A (asymmetric gamma, $k = 1$) and Type S (symmetric normal) distributions $\rho(\tau_c)$ shown in Fig. 13.5. Figure reproduced from [10]

Figure 13.8 shows that the calibrated asymmetric (Type A) distribution for $d = 50$ nm can predict comparable values of hysteretic strain to experiments, where $\varepsilon_{p(\text{hyst})} = 0.9\,\%$ results when the macro stress is cycled from 0 to $\sigma = 1200$ MPa. A proviso is that the cyclic stress is applied after straining the NC metal into the fully plastic regime (>2.5 %). In contrast, the calibrated symmetric (Type S) distribution predicts negligible width ($\varepsilon_{p(\text{hyst})} \sim 0$). A physical explanation is that the asymmetric distribution produces a relatively large fraction of weaker (smaller τ_c) grains and a relatively small fraction of stronger grains. The weaker grains produce a large number of forward events during loading and redistribute internal stress to the stronger grains. During unloading, the stronger grains unload elastically and attempt to restore the polycrystal to the original shape. This drives reverse slip events in the weaker grains.

13.4 Model Application to Lattice Strain Evolution in NC Ni

In this section, we apply the QCP model to investigate the evolution of lattice strains measured by in-situ X-ray diffraction and understand its dependence on grain size. In particular, in-situ X-ray diffraction experiments show that the evolution of residual lattice strain during interrupted uniaxial tension is different for NC vs. coarse-grained (CG) metals [11, 40–43]. The QCP model is applied to identify and understand the conditions to reproduce the experimental diffraction data, including the shift in the position and width of various $\langle hkl \rangle$ diffraction peaks after tensile elongation to various macroscopic strains. The QCP simulations are able to link these X-ray diffraction "footprints" to the violent redistribution of stress at the intergranular scale, the dependence on grain size, the critical stress distribution $\rho(\tau_c)$, and the prior deformation history that precedes the tensile test. The capacity to capture the lattice strain evolution of NC metals provides a robust test of the QCP model.

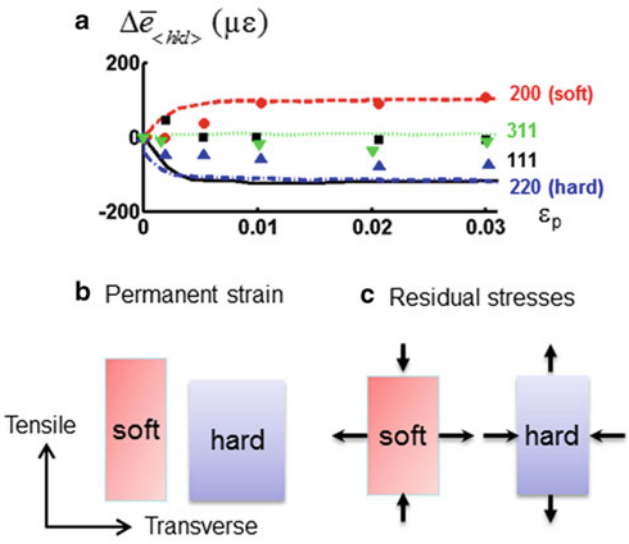

Fig. 13.9 (**a**) The change in residual lattice strain in CG Cu along the transverse direction, as a function of plastic strain (adapted from [44]). These trends can be rationalized from (**b**) the accumulation of a larger axial plastic strain in soft grains under axial tension and (**c**) the development of axial compression and transverse tension in soft grains after unloading. Figure reproduced from [11]

13.4.1 Lattice Strain Evolution in CG vs. NC Ni

For many coarse-grained, elastically anisotropic FCC metals, tensile elongation will shift diffraction peaks due to the deformation anisotropy. In particular, the residual lattice strain along ⟨200⟩ transverse directions increases while that along ⟨220⟩ transverse directions decreases as the imposed tensile elongation is increased. Figure 13.9 confirms these trends for CG Cu [44]. An explanation is that the "family" of FCC grains with a ⟨200⟩ transverse direction has a smaller yield strength in uniaxial tension, on average, while the corresponding ⟨220⟩ family has a larger yield strength on average. The transverse ⟨200⟩ family of grains is therefore soft and accumulates a larger-than-average axial plastic strain during tensile loading (Fig. 13.9b). Upon unloading, the ⟨200⟩ family is overextended plastically and thus tends to have a compressive axial stress and tensile transverse stress. Therefore, the transverse strain for the ⟨200⟩ family tends to increase. The reverse is true for the hard ⟨220⟩ family (Fig. 13.9c).

NC FCC metals do not follow this CG trend. Instead, the measured ⟨*hkl*⟩ families have been reported to exhibit all tensile shifts [42], all compressive shifts [41], or remain unchanged [40]. The varied results were interpreted in terms of a crossover from intragranular slip for larger grains to GB-mediated mechanisms for NC metals.

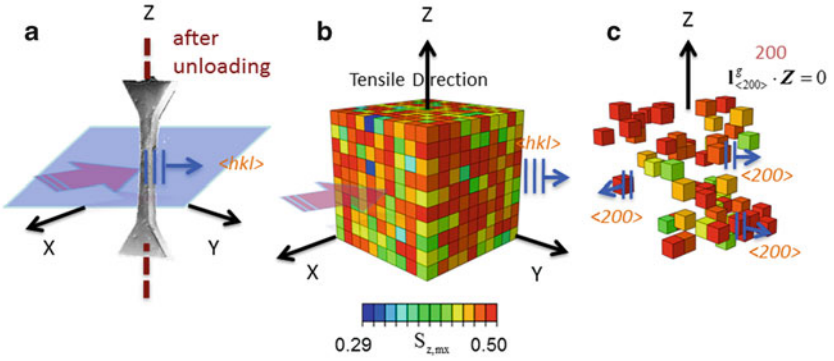

Fig. 13.10 (**a**) A schematic of the in situ X-ray tensile setup. (**b**) A three-dimensional finite element model of a polycrystal with $10 \times 10 \times 10$ grains, each represented by an 8-node brick element. Uniaxial loading/unloading is applied along the Z-direction. Each grain is colored according to the maximum Schmid factor ($S_{z,mx}$) among the 12 FCC slip systems with respect to the loading direction. Numerical values are shown in the color legend. (**c**) An example of a $\langle 200 \rangle$ diffraction group, for which the diffraction vector satisfies $\mathbf{l}^{\mathbf{g}}_{\langle \mathbf{200} \rangle} \cdot \mathbf{Z} = 0$. Figure reproduced from [11]

An alternative view is supported by the application of the QCP model to capture the lattice strain evolution for NC and ultrafine grained (UFG) Ni.

13.4.2 QCP/FE Simulations of In Situ X-ray Diffraction

A combined experimental and modeling effort is made to unveil the deformation mechanisms that lead to the unique NC lattice strain evolution. The experimental measurements of NC lattice strain were obtained by in situ X-ray diffraction performed at the Swiss Light Source (Paul Scherrer Institute (PSI), Switzerland) [45]. Figure 13.10a illustrates the experimental diffraction geometry. Three millimeter dogbone-shaped specimens with a cross section of $200 \times 200\ \mu m^2$ were loaded in tension along the axial (Z) direction at various strain rates $1 \times 10^{-4} \sim 1 \times 10^{-3}\ s^{-1}$ [43]. During testing, an incident X-ray beam along the X direction diffracted and the corresponding diffracted intensities were measured in various directions in the X–Y (transverse) plane, giving the diffraction vector and corresponding lattice strain along transverse $\langle hkl \rangle$ directions. Residual lattice strains were measured after unloading at several points along a stress–strain curve (Fig. 13.11a). Average values were derived from the change in peak position before straining. Electro-deposited NC Ni with a number-averaged grain size $d \sim 30$ nm and a minor out-of-plane 200 texture was investigated.

The QCP model is used to mimic the experimental lattice strains by calculating the elastic strains of subgroup grains that satisfy the diffraction condition. Figure 13.10b shows a QCP/FE model setup with a $10 \times 10 \times 10$ array of 3D cubic finite

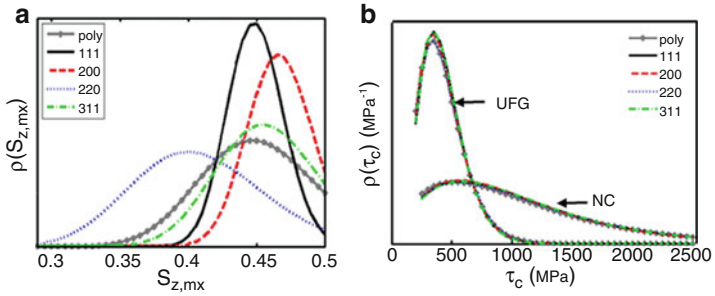

Fig. 13.11 Grain-to-grain probability densities (**a**) $\rho(S_{z,mx})$ for the maximum Schmid factor and (**b**) $\rho(\tau_c)$ for critical resolved shear stress to activate a slip event. Both are shown for the overall polycrystal and for various $\langle hkl \rangle$ families. $\rho(\tau_c)$ is shown for the ultrafine grain (UFG) and nanocrystalline (NC) cases (see Table 13.2 for details). Figure reproduced from [11]

elements (type = C3D8), where each element represents one grain with a particular crystallographic orientation, CRSS τ_c, and a quantized plastic strain jump γ_{target} that can occur on any of the 12 $\langle 110 \rangle / \{111\}$ FCC slip systems. Uniaxial loading and unloading is imposed along the Z direction at a nominal strain rate of 10^{-3}s^{-1}. A *transverse* $\langle hkl \rangle$ diffraction family consists of grains with plane normal $\mathbf{l}_{\langle hkl \rangle}$ perpendicular to the loading axis, similar to the experimental diffraction geometry. In practice, a 2° tolerance in $\mathbf{l}_{\langle hkl \rangle}$ is allowed to reflect the experimental conditions. Figure 13.10c displays a transverse $\langle 200 \rangle$ diffraction family of grains that have a $\langle 200 \rangle$ plane normal satisfying the diffraction condition (i.e., $\mathbf{l}^{\mathbf{g}}_{<\mathbf{200}>} \cdot \mathbf{Z} = 0$.) in the QCP/FE simulations. In the simulations, $\mathbf{l}_{\langle 200 \rangle}$ can lie in any direction in the X–Y plane by assuming that the virtual incident beam can come from any in-plane direction. This increases the grain statistics in the relatively small (1000 grain) simulations.

Two grain sizes are investigated: $d = 30$ nm (NC Ni) and $d = 100$ nm (UFG Ni). Grain orientations are randomly assigned among the 1000 grains. Figure 13.11a shows the resulting grain-to-grain probability distributions $\rho(S_{z,mx})$ for the maximum Schmid factor among the 12 slip systems, assuming a polycrystal with random texture. The average value for all grains is $\overline{S}_{z,mx,\text{poly}} = 0.45$, but a larger value $\overline{S}_{z,mx,\langle 200 \rangle} = 0.47$ is obtained for transverse $\langle 200 \rangle$ grains and a smaller value $\overline{S}_{z,mx,\langle 220 \rangle} = 0.41$ is obtained for *transverse* $\langle 220 \rangle$ grains. The remaining $\langle 311 \rangle$ and $\langle 111 \rangle$ families have intermediate values with $\overline{S}_{z,mx,\langle 311 \rangle} \approx \overline{S}_{z,mx,\text{poly}}$ and $\overline{S}_{z,mx,\langle 111 \rangle} \approx \overline{S}_{z,mx,\text{poly}}$.

Figure 13.11b compares two candidate distributions $\rho(\tau_c)$ for the critical shear stress: a *relatively narrow* one that will be identified with UFG material and a *relatively wide*, *asymmetric* one to be identified with NC material. As noted, the asymmetric $\rho(\tau_c)$ distribution for NC material signifies a large fraction of soft grains that are balanced by a small fraction of hard grains. The $\rho(\tau_c)$ distributions are applied randomly, independent of grain orientation. This is consistent with the concept that the pinning strength is independent of grain orientation. The

simulations may impose a plastic prestrain $\varepsilon_{p(\text{pre})}$ prior to the uniaxial tensile test. The prestrain imposes a pre-existing residual lattice strain, which is known to be high in NC metals. These simulation parameters are summarized in Table 13.2.

Key output quantities are the macroscopic uniaxial stress-plastic strain response $(\sigma - \varepsilon_p)$ for loading, unloading, and reloading, as well as the lattice strain $e_{\langle hkl\rangle,i}$ for each grain i in an $\langle hkl\rangle$ family. The latter is obtained by first computing the components $e_{ij(c)}$ of the elastic strain in terms of the Cauchy stress components $\sigma_{ij(c)}$ and the anisotropic elastic moduli $C_{ijkl(c)}$

$$e_{ij(c)} = C^{-1}_{ijkl}\sigma_{kl(c)},\ \sigma_{kl(c)} = Q_{km}\sigma_{mn(g)}Q_{ln} \tag{13.17}$$

The first equation expresses all quantities in the crystal basis. The second equation determines $\sigma_{ij(c)}$ in terms of the stress components $\sigma_{kl(g)}$ in the fixed global basis and the transformation matrix Q_{km} between the crystal and global bases. Values of $C_{ijkl(c)}$ for Ni are provided in Table 13.2. The lattice strain along the unit normal $\mathbf{l}_{\langle hkl\rangle(c)}$ to $\{hkl\}$ planes is then

$$e_{\langle hkl\rangle} = \mathbf{l}_{\langle hkl\rangle(c)} \cdot \mathbf{e}_{(c)} \cdot \mathbf{l}_{\langle hkl\rangle(c)} \tag{13.18}$$

Finally, the average and deviation in transverse lattice strain among the number $n_{\langle hkl\rangle}$ of grains with a transverse $\langle hkl\rangle$ direction are given by

$$\begin{aligned} \overline{e}_{\langle hkl\rangle} &= \tfrac{1}{n_{hkl}}\sum_{i=1}^{n_{hkl}} e_{\langle hkl\rangle i} \\ s_{\langle hkl\rangle} &= \left(\tfrac{1}{n_{hkl}-1}\sum_{i=1}^{n_{hkl}}\left(e_{\langle hkl\rangle i} - \overline{e}_{\langle hkl\rangle}\right)^2\right)^{1/2} \end{aligned} \tag{13.19}$$

The small sample statistics inherent in 1000 grain simulations are addressed by averaging the results for $\overline{e}_{<hkl>}$ and $s_{\langle hkl\rangle}$ over five instantiations with the same $\rho(\tau_c)$ and $\rho(S_{z,mx,\langle hkl\rangle})$.

13.4.3 Lattice Strain Evolution of NC Ni

Six features are reported from the in situ X-ray diffraction-tensile tests for NC Ni ($d = 30$ nm). Figure 13.12a shows the experimental stress vs. plastic strain response. It is characterized by (I) a large elastic–plastic transition strain ($\varepsilon_{p(\text{trans})} \sim 1\,\%$) and (II) a large hysteretic strain ($\varepsilon_{p(\text{hyst})} \sim 0.2\,\%$) from unloading–reloading. Figure 13.12b shows the change in average transverse residual lattice strain ($\Delta\overline{e}_{<hkl>}$) relative to the beginning of the tensile test. The error bars indicate the standard deviation, based on 100 spectra at each unloaded state. The characteristic trends include: (III) nearly constant average residual lattice strain at smaller plastic

Table 13.2 QCP simulation parameters for NC and UFG Ni

Elast. const. (GPa) [55]	C_{11}: 246.5; C_{12}: 147.3; C_{44}: 124.7
Burgers vector (nm)	b: 0.25
Grain size (nm)	d: 30 (NC); 100 (UFG)
Texture	Random
Schmid factors(avg. of max. in ea. grain)	S_{poly}: 0.45 $S_{\langle 200\rangle}$: 0.47; $S_{\langle 311\rangle}$: 0.46 $S_{\langle 111\rangle}$: 0.45; $S_{\langle 220\rangle}$: 0.41
Quantized pl. strain	$\gamma_{\text{target}} = \min(1.2\ b/d,\ \tau_c/60\ \text{GPa})$ NC: 1.2 $b/d \sim 1\,\%$ UFG: 1.2 $b/d \sim 0.3\,\%$
Crit. stress distrib. (MPa)	$\rho(\tau_c) = \begin{cases} 0 & \tau_c \geq \tau' \\ \dfrac{\tau_c^{k-1}\exp(-\tau_c/\theta)}{\Gamma(k)\theta^k} & \tau_c < \tau_c' \end{cases}$ NC: $\tau_c^{'} = 210, k = 1, \theta = 850$ UFG: $\tau_c^{'} = 200, k = 1, \theta = 220$
Axial plastic prestrain	$\varepsilon_{p(\text{pre})} = -0.5\,\%$

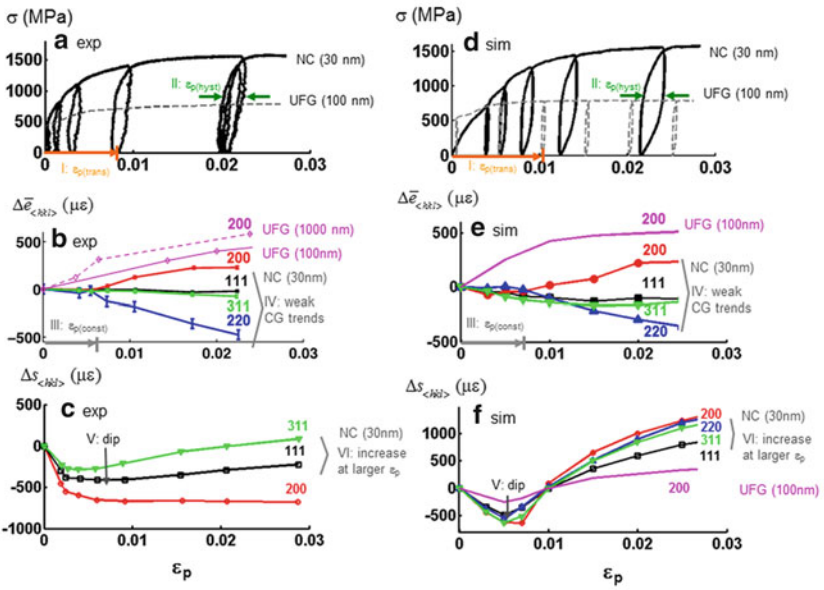

Fig. 13.12 Comparison between in situ X-ray diffraction measurements (**a**–**c**) vs. QCP simulation results (**d**–**f**) for NC and UFG Ni. (**a**, **d**) The stress-plastic strain ($\sigma - \varepsilon_p$) responses. (**b**, **e**) Change in transverse residual lattice strain $\Delta\bar{e}_{\langle hkl\rangle}$ vs. axial plastic strain ε_p. (**c**, **f**) Change in standard deviation in residual transverse lattice strain $\Delta s_{\langle hkl\rangle}$ vs. axial plastic strain ε_p. The experimental UFG data are adopted from [40]. The simulation parameters are shown in Table 13.2. Figure reproduced from [11]

strain (up to $\varepsilon_p \sim 0.6\,\%$); and (IV) CG-like trends at larger strain that are similar to but weaker than for UFG and CG counterparts (i.e., $\Delta\bar{e}_{\langle 200\rangle} > 0$, $\Delta\bar{e}_{\langle 220\rangle} < 0$, and $\Delta\bar{e}_{\langle 111\rangle} \sim \Delta\bar{e}_{\langle 311\rangle} \sim 0$) [44]. In contrast, the UFG response in Fig. 13.12b (e.g., $d = 100$ nm) has no constant region; rather, the residual lattice strains change at the onset of plastic deformation [40]. Figure 13.12c shows the corresponding evolution in lattice strain deviation $s_{\langle hkl\rangle}$ for different diffraction families. Features include: (V) an initial dip at small strain and (VI) a monotonic increase in peak width at larger strain (at least for $\langle 311\rangle$ and $\langle 111\rangle$). In contrast, the experimental peak widths for UFG Ni [46] and CG Cu [47] show no perceptible dip; rather, they gradually increase to a saturation value.

Figure 13.12d–f shows the corresponding QCP simulation results. A comparison of Fig. 13.12a, d shows that the QCP simulations for NC Ni ($d = 30$ nm) can capture the experimental $\sigma - \varepsilon_p$ features (I, II) provided the *wide*, *asymmetric* $\rho(\tau_c)$ distribution (Case NC, Fig. 13.11b) is used. Furthermore, the same distribution is used for all grain orientations and diffraction groups. An axial plastic prestrain ($\varepsilon_{p(\text{pre})} = -0.5\,\%$) is imposed prior to the tensile test. This plastic prestrain is needed to capture the experimental trends in lattice strain in Fig. 13.12b, c. The simulations can also capture the experimental $\sigma - \varepsilon_p$ response for UFG Ni by Cheng et al. [40] if

the more narrow $\rho(\tau_c)$ distribution that is also shifted to smaller values (Case UFG, Fig. 13.11b) is used. In this case, γ_{target} (=0.3 %, Table 13.2) is smaller, as dictated by Eq. (13.15). The same prestrain ($\varepsilon_{p(\text{pre})} = -0.5\,\%$) is used for comparison.

A comparison of Fig. 13.12b, e demonstrates that the QCP simulations (NC 30 nm) capture the experimental diffraction footprints well: the nearly constant average residual lattice strain region (III) and the CG-like trends at larger strain (IV) are reproduced. The QCP simulations for UFG Ni ($d = 100$ nm) do not predict a constant residual lattice strain region, similar to the experimental trends. They predict UFG material to display CG-like trends at smaller strain and larger overall shifts at larger strain relative to NC material. Figure 13.12c, f shows that the QCP simulations (NC 30 nm) qualitatively capture the experimentally observed trends in lattice strain deviation (obtained from peak broadening) vs. imposed plastic strain. This includes the initial dip at a small strain (V) and the monotonic increase in peak width at larger strain (VI). In contrast, the QCP simulations for UFG Ni show a negligible dip at a small strain, similar to experiments.

Some of the experimental NC features are not captured. For instance, the experimental ⟨200⟩ trace in Fig. 13.12b remains flat after the dip but the simulations predict an increase. Also, the ordering of the ⟨*hkl*⟩ curves at large strain is different. We have shown that this discrepancy can be reduced when the same magnitude of axial plastic prestrain (−0.5 %) is imposed by applying biaxial transverse tension rather than the axial compression in the present examples [11]. This highlights the sensitivity of the mechanical and diffraction footprints to plastic prestrain. It also offers an explanation for the variation in experimental lattice strains in NC metals as discussed earlier and as reported in [40–42]. Overall, the comparison of experimental (Fig. 13.12c) vs. simulated (Fig. 13.12f) values of lattice strain deviation is essentially qualitative in nature. In particular, the simulations account primarily for the distribution of internal stress arising from grain-to-grain variations in τ_c and orientation whereas the experimental measurements capture additional contributions to stress from dislocations and other defects. This will have an effect on both the magnitude of the dip and the ordering of the ⟨*hkl*⟩ curves. Unfortunately, current theoretical models are not able to deconvolute all of these contributions.

13.4.4 A Physical View Based on Stress Redistribution

The QCP simulations provide a physical view of NC deformation in terms of the stress redistribution and criticality associated with intragranular slip. Figure 13.13a shows the evolution in residual lattice strain as averaged over the family of all transverse ⟨200⟩ grains, the plastically soft ($\tau_c < \overline{\tau}_c$) subgroup in this family, and the plastically hard ($\tau_c > \overline{\tau}_c$) subgroup ($\overline{\tau}_c =$ the polycrystalline average). Prior to tensile testing, at $\varepsilon_p = 0$, these subgroups have oppositely signed lattice strains. This arises from the axial pre-compression (−0.5 %), which creates residual compressive slip events in soft grains, leaving the soft subgroup in transverse compression and the hard subgroup in transverse tension (Fig. 13.13b). These residual slip events are

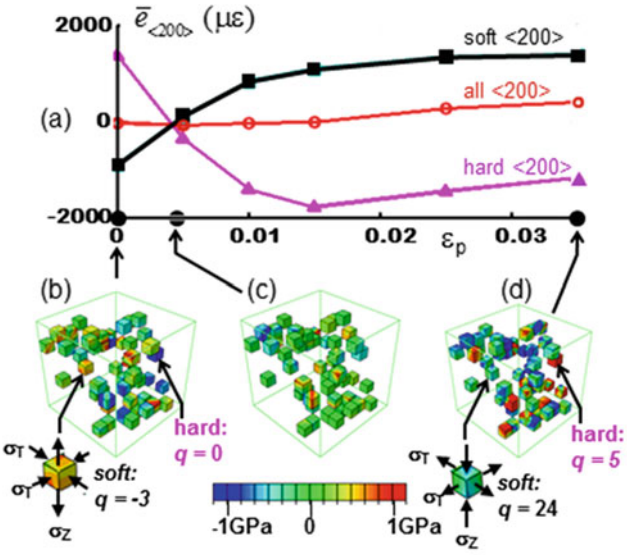

Fig. 13.13 (**a**) QCP simulations of residual transverse lattice strain $e_{\langle 200\rangle}$ vs. macroscopic plastic strain ε_p for the entire transverse $\langle 200\rangle$ family of grains as well as the plastically soft vs. hard subsets in this family. (**b**–**d**) Colored insets of the residual axial stress σ_Z in the transverse $\langle 200\rangle$ family at $\varepsilon_p = 0$, 0.5 %, and 3.5 %, respectively. $q = \#$ of residual slip events in a grain. See Table 13.2 for simulation parameters. Figure reproduced from [11]

removed during the initial stages of the tension test, creating a tensile shift in the soft subgroup and a compressive shift in the hard one. At $\varepsilon_p \sim 0.5\,\%$, the average transverse residual lattice strains $\bar{e}_{\langle 200\rangle}$ for the subgroups converge (Fig. 13.13a) and the corresponding average over the entire $\langle 200\rangle$ family reaches a shallow minimum (Fig. 13.13c). This corresponds to a minimum in the deviation in residual transverse lattice strain (Fig. 13.13b).

During this initial straining from $\varepsilon_p = 0$ to $\sim 0.5\,\%$, the average $\bar{e}_{\langle 200\rangle}$ for the entire $\langle 200\rangle$ family is relatively constant (Fig. 13.13a). This signifies that during initial straining, there is a net transfer of stress between the soft and hard subgroups within the $\langle 200\rangle$ family but not a net transfer of stress between the $\langle 200\rangle$ and other families. Beyond $\varepsilon_p \sim 0.5\,\%$, $\bar{e}_{\langle 200\rangle}$ for the soft and hard subgroups diverge (Fig. 13.13a). This arises primarily from tensile slip events in the soft $\langle 200\rangle$ subgroup. The deviation in residual transverse lattice strain therefore increases (Fig. 13.12f), yet there is little shift in the $\langle 200\rangle$ peak position (Fig. 13.12e). At $\varepsilon_p > \sim 1.5\,\%$, $\bar{e}_{\langle 200\rangle}$ for the $\langle 200\rangle$ family begins to increase, consistent with a weak CG trend. Here, the soft $\langle 200\rangle$ subgroup approaches a maximum tensile shift as the grains within it achieve fully plastic flow. However, $\bar{e}_{\langle 200\rangle}$ for the hard $\langle 200\rangle$ subgroup reverses the trend and begins to increase (Fig. 13.13d). This signifies the onset of a net redistribution in stress between the $\langle 200\rangle$ and other families at larger strain. In particular, plastically soft families with a larger average

Schmid factor (e.g., ⟨200⟩) tend to accumulate more plastic elongation during the tensile test relative to plastically hard families (e.g., ⟨220⟩). This transition from stress redistribution *within families* at smaller strain to stress redistribution *between families* at larger strain also occurs in other diffraction families [11].

If the grain size is increased into the UFG and CG regimes, the quantized plasticity feature diminishes. Further, the number of dislocation nucleation sites in grain interiors increases and the grain-to-grain distribution in τ_c is expected to become more uniform (Fig. 13.11b). These changes diminish the hard vs. soft nature of grains and therefore they reduce stress transfer within ⟨*hkl*⟩ families and shrink the region over which $\bar{e}_{\langle hkl \rangle}$ is constant. The grain-to-grain variation in Schmid factor gains in importance so that the evolution of $\bar{e}_{\langle hkl \rangle}$ with strain is dominated by the stress transfer *between* ⟨*hkl*⟩ families, even during the early stages of the tensile test. For example, the simulations (Fig. 13.12e) show that $\Delta\bar{e}_{\langle 200 \rangle}$ increases with grain size—a trend that is consistent with Cheng et al. [40] and the experimental results for $\Delta\bar{e}_{\langle 200 \rangle}$ in Fig. 13.12b.

The QCP model therefore reproduces the major footprints of the diffraction experiments on NC and UFG Ni and several unique NC properties are rationalized based on intragranular slip rather than GB-accommodation mechanisms. The successful predictions hinge on the assumptions that plastic flow at the grain scale is quantized and that the critical stress for slip takes on a spatially nonuniform, asymmetric grain-to-grain distribution. The quantized slip results in violent stress redistribution. The nonuniform critical stress distribution creates soft and hard grain subgroups, so that a net stress redistribution occurs *within* each diffraction family at smaller strain, and *between* diffraction families at larger strain.

13.5 Conclusions and Future Advances in QCP Modeling

The QCP model illustrates an extension of a conventional crystal plasticity model to successfully capture several unique properties of NC metals. In particular, a new constitutive flow rule is developed based on key observations from atomistic simulations of NC metals. As grain size decreases to the nanometer scale (∼100 nm), the QCP model predicts a transition from continuous and relatively homogenous multiple-dislocation slip to quantized and highly heterogeneous single dislocation slip within grains. This chapter concludes with some key observations about the applications and further development of the model:

- A fit of the QCP model predictions to experimental data suggests that $\rho(\tau_c)$, the grain-to-grain distribution of CRSS for a slip event, is highly positive and skewed, with a larger fraction of relatively soft grains that is offset by an extended tail of relatively hard grains. The present simulations assume that this distribution does not change with plastic deformation and that specific grains retain the same value of τ_c on all 12 FCC slip systems during deformation. Thus, advances in the model might incorporate the evolution of $\rho(\tau_c)$ with strain, including the

possibility that a slip event on a parent slip system in a specific grain changes not only τ_c for a subsequent event on the same system, but also τ_c on other slip systems in the same grain and in neighboring grains. The relative orientation of neighboring grains could be incorporated. In principle, this information could be mined from more fundamental dislocation dynamics studies of single and polycrystalline samples [48, 49].

- The present QCP simulations assume that slip events are driven purely by mechanical stress and that slip occurs instantaneously when the grain-averaged resolved shear stress reaches a critical value. At present, the simulations do not depend on the macroscopic strain rate because τ_c does not change with time and the local strain rate associated with a slip event is assumed to be much larger than the macroscopic rate. However, MD simulations suggest that the *rate-limiting* process for slip events is controlled by the depinning of dislocations from GB ledges [5, 50]. Advances in the model could include a thermally activated feature and utilize transition rate theory with a stress-dependent activation barrier. The strength of GB pinning sites could therefore incorporate a temporal component.
- As the grain size is reduced to <10–20 nm, GB-accommodation mechanisms will be highly interwoven as to affect both the GB structure and stress distribution within grains [8, 51]. Several crystalline-amorphous nanostructures/architectures have been reported to achieve an exceptional combination of strength and ductility by balancing the contributions from dislocation slip and GB accommodation [52, 53]. The QCP model can be modified in principle to capture the effects of both processes by discretizing grains into more elements and incorporating GB sliding [38, 54]. Thermodynamic state variables such as the degree of boundary relaxation could be introduced to qualitatively capture the dependence of GB pinning sites on GB-mediated processes.

References

1. K.S. Kumar, H. Van Swygenhoven, S. Suresh, Mechanical behavior of nanocrystalline metals and alloys. Acta Mater. **51**(19), 5743–5774 (2003)
2. M.A. Meyers, A. Mishra, D.J. Benson, Mechanical properties of nanocrystalline materials. Prog. Mater. Sci. **51**(4), 427–556 (2006)
3. M. Dao, L. Lu, R.J. Asaro, J.T.M. De Hosson, E. Ma, Toward a quantitative understanding of mechanical behavior of nanocrystalline metals. Acta Mater. **55**(12), 4041–4065 (2007)
4. V. Yamakov, D. Wolf, S.R. Phillpot, A.K. Mukherjee, H. Gleiter, Deformation-mechanism map for nanocrystalline metals by molecular-dynamics simulation. Nat. Mater. **3**(1), 43–47 (2004)
5. H. Van Swygenhoven, P.M. Derlet, A.G. Froseth, Nucleation and propagation of dislocations in nanocrystalline fcc metals. Acta Mater. **54**(7), 1975–1983 (2006)
6. H. Van Swygenhoven, J.R. Weertman, Deformation in nanocrystalline metals. Mater. Today **9**(5), 24–31 (2006)
7. J. Schiotz, F.D. Di Tolla, K.W. Jacobsen, Softening of nanocrystalline metals at very small grain sizes. Nature **391**(6667), 561–563 (1998)
8. H. Van Swygenhoven, P.M. Derlet, Grain-boundary sliding in nanocrystalline fcc metals. Phys. Rev. B **64**(22), 224105 (2001)

9. L. Li, P.M. Anderson, M.G. Lee, E. Bitzek, P. Derlet, H. Van Swygenhoven, The stress-strain response of nanocrystalline metals: a quantized crystal plasticity approach. Acta Mater. **57**(3), 812–822 (2009)
10. L. Li, M.-G. Lee, P. Anderson, Critical strengths for slip events in nanocrystalline metals: predictions of quantized crystal plasticity simulations. Metall. Mater. Trans. A **42**(13), 3875–3882 (2011)
11. L. Li, S. Van Petegem, H. Van Swygenhoven, P.M. Anderson, Slip-induced intergranular stress redistribution in nanocrystalline Ni. Acta Mater. **60**(20), 7001–7010 (2012)
12. L. Li, M.-G. Lee, P.M. Anderson, Probing the relation between dislocation substructure and indentation characteristics using quantized crystal plasticity. J. Appl. Mech. **79**(3), 031009 (2012)
13. D. Wolf, V. Yamakov, S.R. Phillpot, A. Mukherjee, H. Gleiter, Deformation of nanocrystalline materials by molecular-dynamics simulation: relationship to experiments? Acta Mater. **53**(1), 1–40 (2005)
14. A.G. Froseth, P.M. Derlet, H. Van Swygenhoven, Dislocations emitted from nanocrystalline grain boundaries: nucleation and splitting distance. Acta Mater. **52**(20), 5863–5870 (2004)
15. D. Farkas, A. Frøseth, H. Van Swygenhoven, Grain boundary migration during room temperature deformation of nanocrystalline Ni. Scr. Mater. **55**(8), 695–698 (2006)
16. Y. Mishin, D. Farkas, M.J. Mehl, D.A. Papaconstantopoulos, Interatomic potential for Al and Ni from experimental data and ab initio calculations. Mater. Res. Soc. Symp. Proc. **538**, 533 (1999)
17. E. Bitzek, P.M. Derlet, P. Anderson, H. Van Swygenhoven, The stress-strain response of nanocrystalline metals: a statistical analysis of atomistic simulations. Acta Mater. **56**(17), 4846–4857 (2008)
18. R.J. Asaro, A. Needleman, Overview no. 42 texture development and strain hardening in rate dependent polycrystals. Acta Metall. **33**(6), 923–953 (1985)
19. D. Peirce, R.J. Asaro, A. Needleman, An analysis of nonuniform and localized deformation in ductile single crystals. Acta Metall. **30**(6), 1087–1119 (1982)
20. S.R. Kalidindi, C.A. Bronkhorst, L. Anand, Crystallographic texture evolution in bulk deformation processing of FCC metals. J. Mech. Phys. Solids **40**(3), 537–569 (1992)
21. D. Peirce, R.J. Asaro, A. Needleman, Material rate dependence and localized deformation in crystalline solids. Acta Metall. **31**(12), 1951–1976 (1983)
22. Y. Shen, P.M. Anderson, Transmission of a screw dislocation across a coherent, non-slipping interface. J. Mech. Phys. Solids **55**(5), 956–979 (2007)
23. C.E. Packard, O. Franke, E.R. Homer, C.A. Schuh, Nanoscale strength distribution in amorphous versus crystalline metals. J. Mater. Res. **25**(12), 2251–2263 (2010)
24. H. Askari, M.R. Maughan, N. Abdolrahim, D. Sagapuram, D.F. Bahr, H.M. Zbib, A stochastic crystal plasticity framework for deformation of micro-scale polycrystalline materials. Int. J. Plast. **68**, 21–33 (2015)
25. M.D. Uchic, D.M. Dimiduk, J.N. Florando, W.D. Nix, Sample dimensions influence strength and crystal plasticity. Science **305**(5686), 986–989 (2004)
26. J.R. Greer, J.T.M. De Hosson, Plasticity in small-sized metallic systems: intrinsic versus extrinsic size effect. Prog. Mater. Sci. **56**(6), 654–724 (2011)
27. J.D. Eshelby, The determination of the elastic field of an ellipsoidal inclusion, and related problems. Proc. R. Soc. Lond. A Math. Phys. Sci. **241**(1226), 376–396 (1957)
28. T. Mura, *Micromechanics of Defects in Solids* (Martinus Nijhoff, The Hague, 1982)
29. Hibbitt, Karlsson & Sorensen Inc., *ABAQUS Reference Manuals* (Hibbitt, Karlsson & Sorensen Inc., Pawtucket, RI, 2005)
30. J.R. Trelewicz, C.A. Schuh, The Hall–Petch breakdown in nanocrystalline metals: a crossover to glass-like deformation. Acta Mater. **55**(17), 5948–5958 (2007)
31. G. Saada, Hall–Petch revisited. Mater. Sci. Eng. A Struct. Mater. **400**, 146–149 (2005)
32. S. Brandstetter, H. Van Swygenhoven, S. Van Petegem, B. Schmitt, R. Maass, P.M. Derlet, From micro- to macroplasticity. Adv. Mater. **18**(12), 1545–1548 (2006)

33. Y.M. Wang, R.T. Ott, T. van Buuren, T.M. Willey, M.M. Biener, A.V. Hamza, Controlling factors in tensile deformation of nanocrystalline cobalt and nickel. Phys. Rev. B **85**(1), 014101 (2012)
34. L. Thilly, S.V. Petegem, P.-O. Renault, F. Lecouturier, V. Vidal, B. Schmitt, H.V. Swygenhoven, A new criterion for elasto-plastic transition in nanomaterials: application to size and composite effects on Cu–Nb nanocomposite wires. Acta Mater. **57**(11), 3157–3169 (2009)
35. F. Ebrahimi, G.R. Bourne, M.S. Kelly, T.E. Matthews, Mechanical properties of nanocrystalline nickel produced by electrodeposition. Nanostruct. Mater. **11**(3), 343–350 (1999)
36. J. Rajagopalan, J.H. Han, M.T.A. Saif, Bauschinger effect in unpassivated freestanding nanoscale metal films. Scr. Mater. **59**(7), 734–737 (2008)
37. J. Rajagopalan, J.H. Han, M.T.A. Saif, Plastic deformation recovery in freestanding nanocrystalline aluminum and gold thin films. Science **315**(5820), 1831–1834 (2007)
38. Y.J. Wei, A.F. Bower, H.J. Gao, Recoverable creep deformation and transient local stress concentration due to heterogeneous grain-boundary diffusion and sliding in polycrystalline solids. J. Mech. Phys. Solids **56**(4), 1460–1483 (2008)
39. X.Y. Li, Y.J. Wei, W. Yang, H.J. Gao, Competing grain-boundary- and dislocation-mediated mechanisms in plastic strain recovery in nanocrystalline aluminum. Proc. Natl. Acad. Sci. U. S. A. **106**(38), 16108–16113 (2009)
40. S. Cheng, A.D. Stoica, X.L. Wang, Y. Ren, J. Almer, J.A. Horton, C.T. Liu, B. Clausen, D.W. Brown, P.K. Liaw, L. Zuo, Deformation crossover: from nano- to mesoscale. Phys. Rev. Lett. **103**(3), 4 (2009)
41. Y.M. Wang, R.T. Ott, A.V. Hamza, M.F. Besser, J. Almer, M.J. Kramer, Achieving large uniform tensile ductility in nanocrystalline metals. Phys. Rev. Lett. **105**(21), 215502 (2010)
42. H.Q. Li, H. Choo, Y. Ren, T.A. Saleh, U. Lienert, P.K. Liaw, F. Ebrahimi, Strain-dependent deformation behavior in nanocrystalline metals. Phys. Rev. Lett. **101**(1), 4 (2008)
43. S. Van Petegem, L. Li, P.M. Anderson, H. Van Swygenhoven, Deformation mechanisms in nanocrystalline metals: insights from in-situ diffraction and crystal plasticity modelling. Thin Solid Films **530**, 20–24 (2013)
44. B. Clausen, T. Lorentzen, T. Leffers, Self-consistent modelling of the plastic deformation of FCC polycrystals and its implications for diffraction measurements of internal stresses. Acta Mater. **46**(9), 3087–3098 (1998)
45. H. Van Swygenhoven, B. Schmitt, P.M. Derlet, S. Van Petegem, A. Cervellino, Z. Budrovic, S. Brandstetter, A. Bollhalder, M. Schild, Following peak profiles during elastic and plastic deformation: a synchrotron-based technique. Rev. Sci. Instrum. **77**(1), 10 (2006)
46. Z. Budrovic, S. Van Petegem, P.M. Derlet, B. Schmitt, H. Van Swygenhoven, E. Schafler, M. Zehetbauer, Footprints of deformation mechanisms during in situ x-ray diffraction: nanocrystalline and ultrafine grained Ni. Appl. Phys. Lett. **86**(23), 3 (2005)
47. Z. Budrovic, H. Van Swygenhoven, P.M. Derlet, S. Van Petegem, B. Schmitt, Plastic deformation with reversible peak broadening in nanocrystalline nickel. Science **304**(5668), 273–276 (2004)
48. F.F. Csikor, C. Motz, D. Weygand, M. Zaiser, S. Zapperi, Dislocation avalanches, strain bursts, and the problem of plastic forming at the micrometer scale. Science **318**(5848), 251–254 (2007)
49. V.V. Bulatov, W. Cai, *Computer Simulations of Dislocations* (Oxford University Press, Oxford, 2006)
50. C. Brandl, P.M. Derlet, H.V. Swygenhoven, Dislocation mediated plasticity in nanocrystalline Al: the strongest size. Model. Simul. Mater. Sci. Eng. **19**(7), 074005 (2011)
51. T.J. Rupert, D.S. Gianola, Y. Gan, K.J. Hemker, Experimental observations of stress-driven grain boundary migration. Science **326**(5960), 1686–1690 (2009)
52. Y.M. Wang, E. Ma, Three strategies to achieve uniform tensile deformation in a nanostructured metal. Acta Mater. **52**(6), 1699–1709 (2004)
53. Y. Wang, J. Li, A.V. Hamza, T.W. Barbee, Ductile crystalline–amorphous nanolaminates. Proc. Natl. Acad. Sci. **104**(27), 11155–11160 (2007)

54. Y.J. Wei, L. Anand, Grain-boundary sliding and separation in polycrystalline metals: application to nanocrystalline fcc metals. J. Mech. Phys. Solids **52**(11), 2587–2616 (2004)
55. H.B. Huntington, The elastic constants of crystals. Solid State Phys. Adv. Res. Appl. **7**, 213–351 (1958)